Proceedings of the 2019 Hypervelocity Impact Symposium
HVIS2019
April 14-19, 2019, Destin, FL, USA
HVIS2019-DSA2017

Coils, Codes and Comets: My Attempts to Partially Understand Some Particular Aspects of Hypervelocity Impacts

David A. Crawford*

Crawford Technical Services, LLC, Winona, Minnesota, USA

Abstract

At the time of this writing in 2019, I have been studying hypervelocity impacts for about 34 years. I attended my first Hypervelocity Impact Symposium in 1992. In this paper, I attempt to show what I've been up to all this time but also show some of the things I've learned along the way. I've singled out three topics that stand out in my mind as milestones in my career: the impact of Comet Shoemaker-Levy 9 on Jupiter in 1994, the development of adaptive mesh refinement for the CTH hydrocode in 1998-2001 and my ongoing studies of hypervelocity impact-generated magnetic fields from 1985 to the present day.

Keywords: Shoemaker-Levy 9, Jupiter, adaptive mesh refinement, AMR, CTH, magnetism, paleomagnetism, Moon

1. Introduction

The impact of Comet Shoemaker-Levy 9 on Jupiter in July, 1994 was the largest, most energetic impact event on a planet ever witnessed. Because it broke up during a close encounter with Jupiter in 1992, it was bright enough to be discovered more than a year prior to impact, allowing the scientific community an unprecedented opportunity to assess the effects such an event would have. Many excellent observations were made from Earth-based telescopes, the Hubble Space Telescope (HST) and the Galileo spacecraft en route to Jupiter. In 1993 and 1994, my Sandia colleagues and I performed simulations prior to the impact that compared well qualitatively with many of the observations. After the impact event, we used the observations in conjunction with CTH computational simulations to determine the sizes of the fifteen fragments that made discernible impact features on the planet and from that made an estimate of the total size and energy of the impact event.

In 1998-2001, I implemented an adaptive mesh refinement capability into CTH. The adaptivity is block-based with refinement and un-refinement occurring in an isotropic 2:1 manner. The capability, like CTH, is designed to run on serial, multiprocessor and massively parallel platforms. By 2001, we could run large, parallel 3D AMR calculations that realized about an order of magnitude decrease in CPU requirements over non-AMR counterparts. The fastest available computers at the time required 3D calculations to be of a heroic nature even with AMR. The advance of computing hardware in the past decade, however, has enabled routine 3D calculations with AMR to become a staple of very large CTH calculations. The surprising thing, however, is the much greater performance advantage we're seeing on certain types of AMR problems – in some cases, by two or three orders of magnitude. Credit for this, I think is partly due to the unique approach we use in CTH for the definition of refinement indicators. Rather than a more automated approach, we require analysts to construct indicators in their input decks using a simple construct of operators, filters, database variables and thresholds.

* Corresponding author. Tel.: 1-507-459-0659
E-mail address: dave_crawford@q.com.

The origin and evolution of the Moon's magnetic field has been a major question in lunar science ever since Luna 1 made the first magnetic measurements in the vicinity of the Moon in 1959. Orbital measurements show that the magnetic field at the surface of the Moon has local scale lengths on the order of 1-100 km but correlation with specific geologic features remains elusive. The source of the anomalies from an internal core dynamo or from exogenic processes such as impact, remains a key question. In my earliest work, I showed that impact-generated magnetic fields showed promise in explaining the magnetism of lunar samples particularly and perhaps the "jumbled" magnetic state of the lunar surface today. In my most recent work, I show that craters at nearly all scales may leave behind remnant magnetic fields observable at the surface or in samples. For at least five large basins on the Moon, simulated anomalies are similar enough to orbital magnetic field data for us to conclude there is an alternative explanation for many lunar anomalies that doesn't require the presence of a lunar dynamo. At least some anomalies may be associated with magnetization acquired by rocks in the presence of the transient magnetic field produced by the impact itself.

2. Numerical simulations of the impact of Comet Shoemaker-Levy 9 on Jupiter

In early July, 1992, periodic comet Shoemaker-Levy 9 broke up during a close encounter with Jupiter (Fig. 1). For a brief two-year period, about 20 large fragments and associated debris followed one last orbit about Jupiter before striking the planet at an estimated velocity of 60 km/s. The largest fragments entered the Jovian atmosphere during the week of July 16-22, 1994. Although the impact sites were located just beyond the limb of Jupiter and were not directly visible from Earth, the Galileo spacecraft was positioned for direct viewing of the impact sites. While impact phenomena were not spatially resolved by the spacecraft, its timing, spectral and luminosity data are invaluable for comparison with analytical and numerical models. Fireballs and plumes generated by the impacts were visible in line-of-sight from Earth within a minute and the impact locations themselves rotated into view within 7-20 minutes [1]. The wealth of data provided by this fortuitous event gave us an opportunity to assess models of meteoroid entry into planetary atmospheres and to estimate the size of the Shoemaker-Levy 9 parent body based on observations of the radiated light flux observed by the Galileo spacecraft and by Earth-based telescopes.

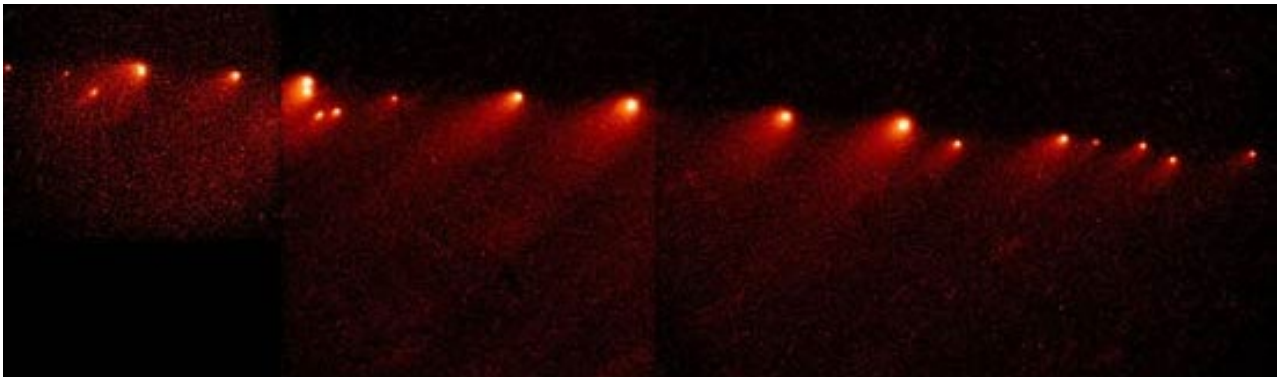

Fig. 1. Comet Shoemaker-Levy 9 soon after its discovery in 1993 (Hubble Space Telescope Science Institute: see [1]). The fragments were labeled A through W. Some disappeared from view (e.g. J, M and P1) and some split (e.g. Q1, Q2).

Simulations performed prior to the impact of Comet Shoemaker-Levy 9 using the CTH shock-physics code [2] compare well qualitatively with many of the observations [3-5]. Nevertheless, good quantitative models of the event were required in order to extract useful information from observations of the events. Fortunately, models were strongly constrained by the excellent data collected (Fig. 2), especially: (1) the direct light-flux observations made by the Galileo spacecraft [6]; (2) the pattern of dark ejecta the impacts left in the Jovian stratosphere which varied considerably in albedo and lateral extent [1, 7]; and (3) the Earth-based telescope observations of the infrared impact light flashes [8]. By using a semi-analytical meteoroid entry model [9] as initial conditions for plume evolution models we could investigate the Shoemaker-Levy 9 events in the context of matching visible and infrared light fluxes (Fig. 3). We performed simulations for ten test cases with comet fragments ranging in size from 250 to 1250 m in diameter. In all cases, we assumed the comets were of density 0.95 g/cm^3 or 0.25 g/cm^3 with an equation-of-state (including melting, vaporization, dissociation and ionization) appropriate for water ice. A two-dimensional representation, symmetric to the 45° entry angle, was used to simulate the first few minutes of fireball evolution in CTH. Output light curves were computed using opacity appropriate for the Jovian atmosphere [10] and compared against Galileo spacecraft observations (Fig. 3).

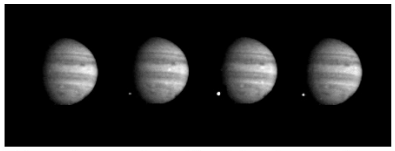

Meteoric entry in visible light observed by Galileo Spacecraft en route to Jupiter (NASA)

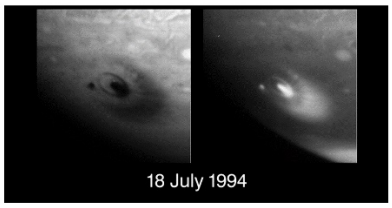

Dark ejecta left by the impacts faded gradually over days/weeks. (Hubble Space Telescope Science Institute)

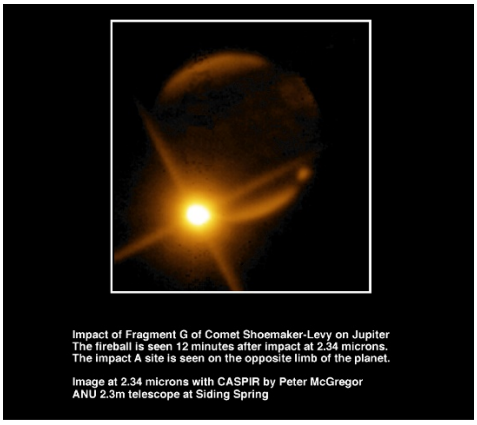

Earth-based telescopic observations of the re-entering ejecta were bright in the infrared (Siding Spring Observatory)

Fig. 2. Representative data collected during the impacts of Comet Shoemaker-Levy 9 on Jupiter in 1994 [1,6-8,11-14].

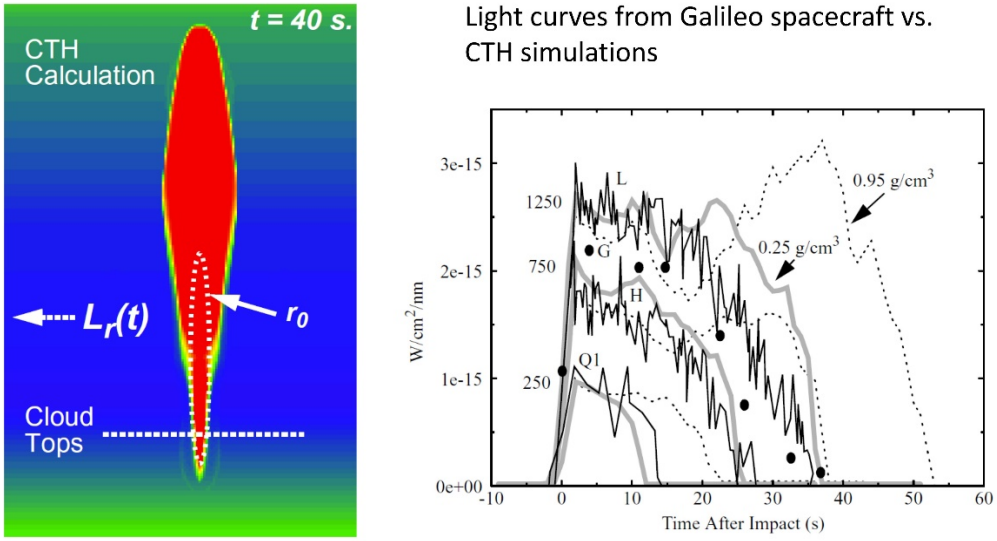

Fig. 3. A modified version of CTH was run with input from a semi-analytical entry model we developed [9] and using the Jovian atmospheric opacity model of [10]. Output light curves (L_r) were compared to Galileo spacecraft observations of the L, H and Q1 impacts (black lines) and the G impact (black dots) [6] to determine impactor size and density. CTH light curves from 250, 750 and 1250 m impactors are shown. The best matching light curves resulted from low density (0.25 g/cm^3) impactors (gray curves).

Table 1. Shoemaker-Levy 9 fragment size estimates (from [9]).

Fragment*	HST Class†	2.3 μm Peak (Jy)‡	12 μm Peak (Jy)‡	Diameter (m)♦
A	2a	20	1,200	450
B	3			(50)
C	2a	25		380
D	3	4		200
E	2a	100	1,550	610
G	1	460		1,000•
H	2a	100	2,400	660•
K	1	460		1,000•
L	1	1,000	12,700	1,270•
N	3	0.04		45•
Q2	3			(50)
Q1	2b	90	1,700	600•
R	2b	70	990	530
S	2c	120		640
W	2c	60		490•
Parent	-	-	-	1,400¶

*Fragments F, P2, T, U and V produced no discernible impact features. Fragments J, M and P1 faded from view before impact [7]. The letters I and O were not used.

†Based on first view of the impact site with the Hubble Space Telescope [7]. Class 1 = large dark feature (>10,000 km radius), Class 2 = medium dark feature (4000-8000 km radius), Class 3 = small dark feature (<3000 km radius).

‡Observed light flux of the main infrared event seen from Earth at 2.3 and 12 μm [8, 11-13].

♦Diameter is estimated from a least-squares analysis incorporating Galileo light-flux observations (marked with • symbol and calibrated against CTH light-output calculations) and assuming r^3 dependence of the peak flux (for a given wavelength) observed from Earth-based telescopes [8]. Values in parentheses are estimates assuming diameter equivalence within HST class 3. Uncertainty (1 σ) of individual fragment diameter is 15% for fragments A, E, H, L, Q1 and R and 30% for fragments B, C, D, G, K, N, Q2, S and W. Best fitting fragment density is about 0.25 g/cm^3.

¶Assuming a density of 0.5 g/cm^3 before breakup in 1992. The total volume of the fragments would make a sphere 1760 m in diameter (at 0.25 g/cm^3). Uncertainty of these estimates is dominated by uncertainties of the largest fragments (L, K and G), about 25%.

Table 1 shows our estimated sizes for the Shoemaker-Levy 9 fragments that produced discernible features on the planet. The fragment diameter is estimated from a least-squares analysis incorporating Galileo light-flux observations (calibrated against CTH light-output calculations) and assuming r^3 dependence (mass scaling) of the peak flux for a given wavelength observed from Earth-based telescopes [8, 11-13]. For fragments that produced the smallest impact features on the planet, we assumed a constant diameter within the site classification derived from HST imagery [7]. For most cases where sufficient overlap between the Galileo and Earth-based observations exists, the r^3 scaling law holds fairly well. Normal variations due to density heterogeneity among the fragments is expected. There are a couple of notable exceptions, however. Fragments Q1 and W were relatively small by Galileo light flux estimates but of moderate size based on Earth-based observations. This could be explained if they were denser than the other fragments (e.g. fully dense silicate vs. fluffy, muddy water ice).

The fragments of Shoemaker-Levy 9 that hit Jupiter with discernible effect have a total volume that would make a 1.8±0.5 km diameter sphere at an average density of 0.25 g/cm^3. This is consistent with the total volume of dusty debris seen on the planet after the impacts, corresponding approximately to a 1-km diameter sphere [14], assuming a typical debris particle density of (1-2 g/cm^3). With a pre-breakup density of 0.5 g/cm^3 [15-16], the parent body had a diameter of 1.4±0.4 km. With these parameters, the Shoemaker-Levy 9 family pummeled Jupiter with the energy equivalent of 300 Gigatons of TNT.

3. The development of adaptive mesh refinement (AMR) in CTH

Adaptive mesh refinement (AMR) has been used for improving computational resolution when resources are limited and has been used for hyperbolic problems on an experimental basis for years. For a mature Eulerian multi-material shock-physics code family like CTH and its predecessors, adaptivity was a natural next step in code development. By 1998, CTH had been running on the largest parallel machines in the world. At around that time, I performed a scaling study by adding AMR to a simple 2D ideal gas hydrocode and determined we should be able to realize an order of magnitude improvement in performance on many large parallel 3D calculations if we adopted AMR for CTH. I proposed this to Gene Hertel, who was the CTH project lead at the

time. With his go ahead and support from Paul Yarrington who was my manager at the time, we started what turned into a three-year effort to put AMR into CTH.

In order to achieve adaptivity yet retain the man-years of effort that have been expended on the development of physics routines, the AMR in CTH is block-based, where each block consists of a small patch of cells (typically 8x8x8 or 10x10x10). In order to facilitate its implementation on massively parallel platforms, each block communicates with its neighbors using a generalization of the message-passing paradigm developed for multiprocessor CTH. A maximum 2:1 resolution difference across block boundaries is strictly enforced. Block refinement and un-refinement is isotropic. In multiprocessor AMR-CTH calculations, blocks are distributed across processors and CPU loading is optimized.

By 2001, we could run large, parallel 3D AMR calculations that realized about an order of magnitude decrease in CPU requirements over non-AMR counterparts (see Fig. 4a). The fastest available computers at the time required 3D calculations to be of a heroic nature even with AMR. The advance of computing hardware in the past decade, however, has allowed AMR to become a staple routine of very large CTH calculations. Extrapolating the curve in Figure 4a and assuming a doubling of CPU memory and performance every 18 months would suggest that AMR calculations would improve their performance advantage over non-AMR calculations by about a factor of two every ten years. Today, therefore, we expect to see a 30-40 times performance advantage for AMR vs. non-AMR. The surprising thing, however, is the much greater performance advantage we're seeing on other types of AMR problems – in some cases, by two or three orders of magnitude. Credit for this, I think is partly due to the unique approach we use in CTH for the definition of refinement indicators. Rather than an automated approach, we require analysts to construct indicators in their input decks using a simple construct of operators, filters, database variables and thresholds. While this is more work for them, it allows maximum flexibility and puts more control of computational resources into their hands. The analyst is, after all, the most likely person to know where to focus refinement to achieve their goals.

Figure 4b shows an example of an AMR calculation which exhibits a 200-300 times performance advantage over its non-AMR counterpart. It is a simulation of the hypothesized formation of the Moon by the impact of a Mars-sized body on the proto-Earth. Because of the importance of the large volume of vapor produced during the impact, the most effective adaptive meshing strategy is to maintain equal mass zoning as much as possible. In this way, CTH with AMR can realize some of the efficiencies of Lagrangian mesh free methods such as SPH (the typical method used on this type of problem) while capturing features more accurately represented by Eulerian methods (e.g. shocks in gases).

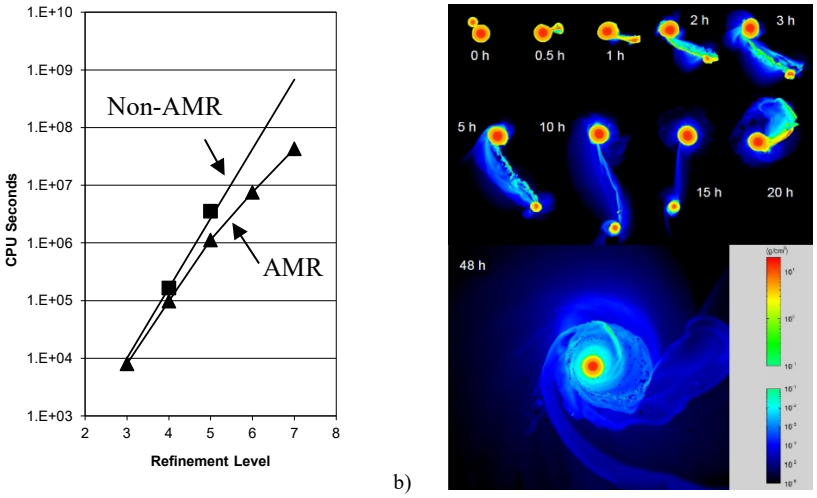

a) b)

Fig. 4. a) CPU timing study comparing AMR vs. Non-AMR methods on a heroic problem in 2001. At highest resolution, the AMR calculation outperformed the Non-AMR calculation by a factor of 10. b) Recent high-resolution AMR-CTH simulation of a Mars-sized object striking the proto-Earth in a candidate Moon forming impact (from [19]). Time after impact (in hours) is shown for each panel. This AMR calculation required approximately 40 million zones, including ghost cells and was run on 256 processors for six days. The non-AMR equivalent would need at least 20 billion zones – nearly 500 times the memory and 200-300 times the CPU requirements of the AMR calculation.

4. Studying magnetic and electric fields (and separated electric charge) caused by hypervelocity impacts

The origin and evolution of the Moon's magnetic field has been a major question in lunar science ever since Luna 1 made the first magnetic measurements in the vicinity of the Moon in 1959. Orbital measurements show that the magnetic field at the surface of the Moon has local scale lengths on the order of 1-100 km. While this could suggest a correlation with impact craters, most lunar magnetic anomalies don't appear to correlate with known geologic structures, including impacts. Nevertheless, the question of lunar magnetism has been a strong motivator for this work from the time when I started studying impact-generated magnetic fields to the present day [20-25]. And now, with my most recent work, I can explain why magnetic anomalies don't generally correlate with impact structures even if produced by impact events. Because lunar materials have relatively low thermoremanence susceptibility, impacts produce magnetic fields observable in orbital magnetic field data only for large and relatively rare impact craters - large lunar basins greater than ~200 km diameter. If occurring in thick units with higher thermoremanence susceptibility, craters as small as 50-100 km may produce orbital anomalies but this would also be a relatively rare occurrence [25].

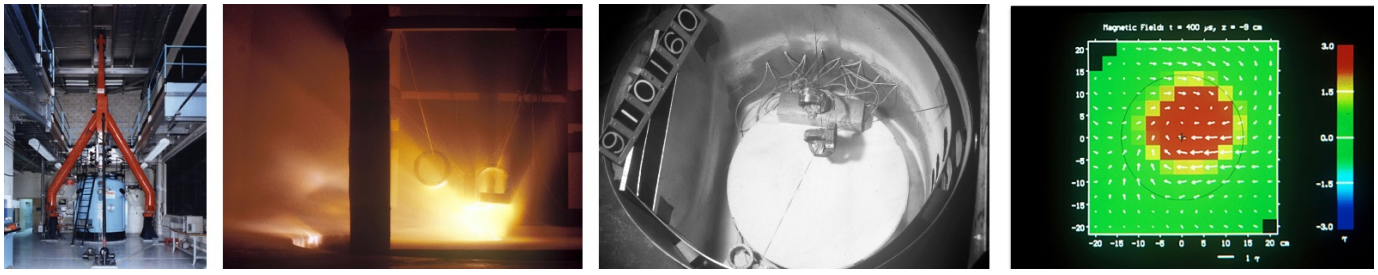

Fig. 5. From left-to-right: the NASA Ames Vertical Gun Range; a time exposure of a hypervelocity impact into powdered dolomite with magnetic search coils position above and below the target surface; a mu-metal shielded target was used in later experiments to reduce the ambient magnetic field to lunar-like conditions (~450 nT) with carefully wrapped and shielded magnetic search coils designed to reduce electrostatic noise; a map of the magnetic field observed 400 micro-seconds after the vertical impact of a 1/4 inch Al sphere at 5 km/s.

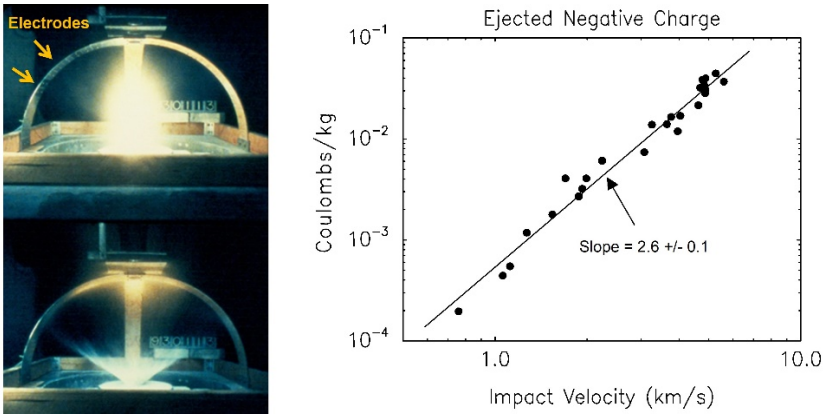

Fig. 6. Apparatus used to measure electrostatic charge separation during a hypervelocity impact event (left) at the NASA AVGR. The moment-of-impact is shown in the top frame, ejecta curtain development shown in the bottom frame. The total charge carried out of the crater by the ejecta scales linearly with projectile mass and has a $v^{2.6}$ dependence on velocity (right) [23].

In 1985, during my junior year at Brown University, Pete Schultz introduced me to the question of impact-generated magnetic fields. Starting then, and during my graduate studies with Pete thereafter, I pursued the study of impact-generated magnetic fields by primarily using the experimental facilities of the NASA Ames Vertical Gun Range (AVGR) (Fig. 5). These studies culminated with the unambiguous mapping of impact-generated magnetic fields during hypervelocity impact which we published in the HVIS proceedings in 1992 [22]. After this work was completed, I decided to attempt an understanding of the strong electrostatic noise signals that had always bedeviled our magnetic measurements. It was really these measurements of the electrostatics (how static electric charges were created and moved about the target during a hypervelocity impact) that informs our understanding of the

magnetic field production mechanism. In the publication of the 1998 HVIS Proceedings [23], we showed how the quantity of electric charged produced during hypervelocity impact scaled with the mass and velocity of the impactor (Fig. 6) and how impact-generated magnetic fields should increase linearly with the radius of the projectile. In the 20 years since that publication, I tinkered with theoretical models based on plasma sheath theory to better understand the charging mechanism. This culminated in the publication in the 2015 HVIS Proceedings of a model implemented into CTH and validated against the earlier experimental data [24]. This model was general enough to allow us to extrapolate to large natural crates on the Moon. Combined with modifications to CTH to compute 3D magnetic fields and capture remanence, we now have the ability to predict magnetic anomalies from natural impact events on the Moon (Figs. 7 and 8) and elsewhere throughout the solar system.

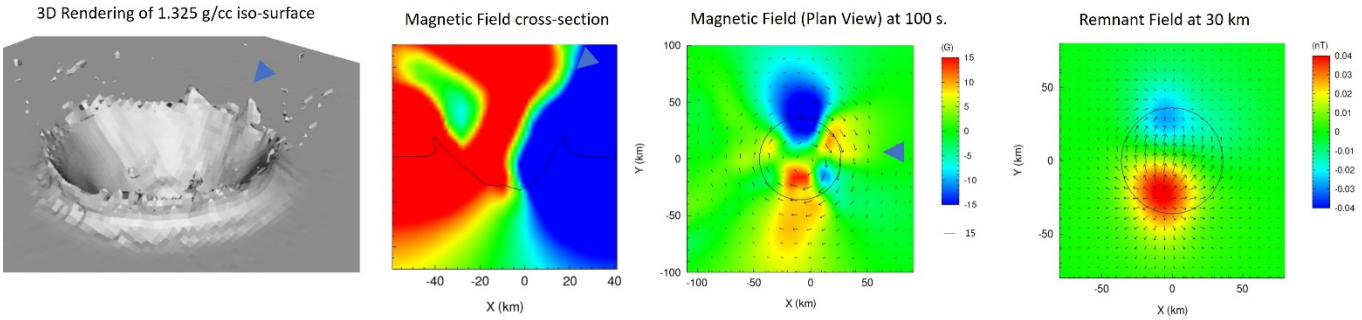

Fig. 7. CTH simulation of a 72-km central-peak crater on the Moon 100 seconds after impact. From left-to-right: 3D rendering of the 1.325 g/cc density iso-surface, Y-component of the magnetic field in cross section, all components of the magnetic field (horizontal components depicted with arrows, vertical component with color) looking from above. Magnetic field strength shown in Gauss (1G = 10^{-4} Tesla). Pre-impact projectile trajectory indicated by the blue triangles and final crater rim indicated by circles. At far right, the remnant field that would be observed today at 30 km altitude. (modified from [25]).

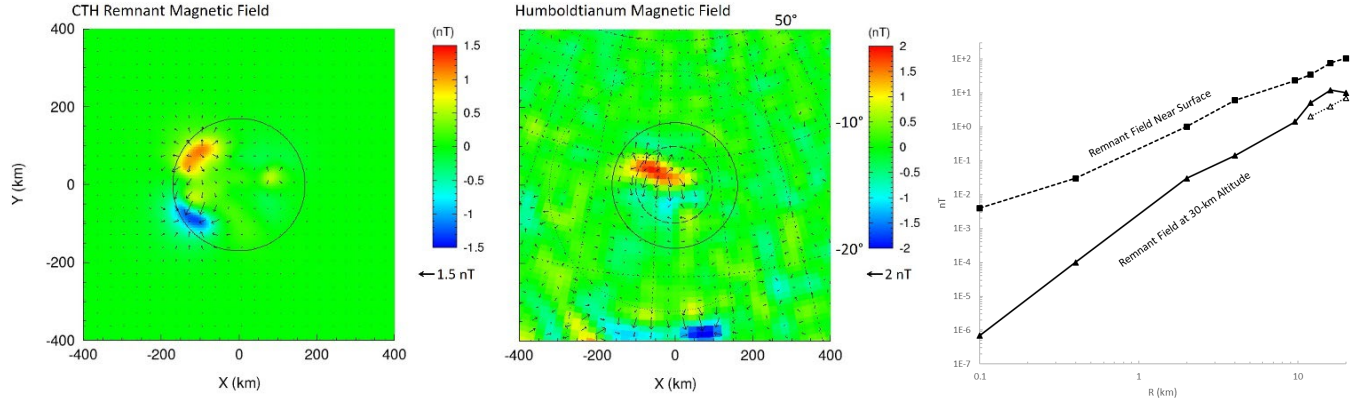

Fig. 8. From left-to-right: CTH simulation of a 340-km crater, the magnetic anomaly of the 322-km lunar basin Humboldtianum, and a plot of remnant magnetic field intensity near the surface and at 30-km altitude for a range of projectile radii. Only the largest projectiles (10 km radii and larger) which produce basins larger than 200 km in diameter will produce strong enough anomalies to be observable from orbit with present technology. (modified from [25])

Acknowledgements

I am grateful to the following individuals with whom I have co-authored papers and technical reports during the course of my hypervelocity impact career: Olivier Barnouin, Amy Barr, Ray Bell, Mark Boslough, Aaron Brundage, Robert Butler, Robin Canup, Mark Cintala, Millie Elrick, Eric Harstad, Dave Hensinger, Gene Hertel, Marlin Kipp, Charles Mader, Sharon Petney, Sue Phelps, Betty Pierazzo, Stephanie Quintana Bouchey, Allen Robinson, Kevin Ruggirello, Bob Schmitt, Pete Schultz, Shane Schumacher, Jim Simmons, Angela Stickle, Paul Taylor, Tim Trucano and Kelly Wrobel.

I want to single out several of the individuals mentioned above. Foremost, I want to thank my friend and colleague and PhD advisor, Pete Schultz. He continues to inspire me to pursue impact-generated magnetic fields and other questions of planetary impact science. Secondly, I want to recognize some of my many colleagues at Sandia. I worked with Mark Boslough extensively

on Shoemaker-Levy 9. He was a principal influence during my earliest days at Sandia. I am grateful to several core members of the CTH development team: Gene Hertel, Bob Schmitt, Eric Harstad and Paul Taylor. Gene in particular has been a personal mentor and a tireless advocate of CTH when he was the team lead in the 1990s right up to the present day.

References

[1] Hammel, H. B. et al., 1995, HST Imaging of Atmospheric Phenomena Created by the Impact of Comet Shoemaker-Levy 9, *Science, 267*, 1288-1296.

[2] McGlaun, J. M, Thompson S. L. and Elrick, M. G., 1990, CTH - A Three-Dimensional Shock-Wave Physics Code, *International Journal of Impact Engineering, Vol. 10*, p. 351.

[3] Boslough, M. B., Crawford, D. A., Trucano, T. G. and Robinson, A. C., 1994, Watching for Fireballs on Jupiter, *EOS Transactions, American Geophysical Union, Vol. 75, Issue 27, pp. 305-310.*

[4] Crawford, D. A., Boslough, M. B., Trucano, T. G. and Robinson, A. C., 1994, The impact of comet Shoemaker-Levy 9 on Jupiter, *Shock Waves, 4*, pp. 47-50.

[5] Crawford, D. A., Boslough, M. B., Trucano, T. G. and Robinson, A. C., 1995, The Impact of Comet Shoemaker-Levy 9 on Jupiter, *International Journal of Impact Engineering*, pp. 253-262.

[6] Chapman, C. R., 1996, Galileo observations of the impacts, in *The Collision of Comet Shoemaker-Levy 9 and Jupiter*, K. S. Noll, H. A. Weaver and P. D. Feldman, eds., Cambridge Univ. Press, 121-132.

[7] Hammel, H. B., 1996, HST imaging of Jupiter shortly after each impact: Plumes and fresh sites, in *The Collision of Comet Shoemaker-Levy 9 and Jupiter*, K. S. Noll, H. A. Weaver and P. D. Feldman, eds., Cambridge Univ. Press, 111-120.

[8] Nicholson, P. D., 1996, Earth-based observations of impact phenomena, in *The Collision of Comet Shoemaker-Levy 9 and Jupiter*, K. S. Noll, H. A. Weaver and P. D. Feldman, eds., Cambridge Univ. Press, 81-109.

[9] Crawford, D. A., 1997, Comet Shoemaker-Levy 9 Fragment Size Estimates: How big was the Parent Body?, in *Near-Earth Objects, The United Nations International Conference,* John L. Remo, ed., Annals of the New York Academy of Sciences, Vol 822, pp. 155-173.

[10] Nemtchinov, I. V. et al., 1996, Spectral Opacities and Ablation Rates for Recognized Meteoroid Materials, Interim Report 001 on task 1.0 under the Sandia National Laboratories Contract AS-6889, Institute for Dynamics of Geospheres, Russian Academy of Sciences, Moscow, 136 pp.

[11] Lagage, P. O. et al., 1995, SL-9 fragments A, E, H, L, Q1 collision on to Jupiter: Mid-infrared light curves*, Geophys. Res. Lett., 22*, 1773.

[12] Takeuchi, S. et al., 1995, Near-IR imaging observations of the cometary impact into Jupiter: Time variation of radiation from impacts of fragments C, D and K, *Geophys. Res. Lett., 22*, 1581.

[13] McGregor, P. et al. 1996, CASPIR observations of the collision of Comet Shoemaker-Levy 9 with Jupiter, *Icarus, 121*, 361-388.

[14] West, R. A., 1996, Particulate matter in Jupiter's atmosphere from the impacts of Comet P/Shoemaker-Levy 9, in *The Collision of Comet Shoemaker-Levy 9 and Jupiter*, K. S. Noll, H. A. Weaver and P. D. Feldman, eds., Cambridge Univ. Press, 269-292.

[15] Scotti, J. V. and Melosh, H. J., 1993, Tidal Breakup and Dispersion of P/Shoemaker-Levy 9: Estimate of Progenitor Size, *Nature, 365*, 7333.

[16] Asphaug, E. and Benz, W., 1994, Density of Comet Shoemaker-Levy 9 deduced by modelling breakup of the parent 'rubble pile', *Nature*, *370*, 120-124.

[17] Crawford, D. A., Taylor, P. A., Bell, R. L. and Hertel, E. S., 2002, Adaptive Mesh Refinement in the CTH Shock Physics Hydrocode, *New Models and Hydrocodes for Shock Wave Processes in Condensed Matter,* Edinburgh, U.K., May 19-24, 6 pages.

[18] Canup, R. M., Barr, A. C. and Crawford, D. A., 2013, Lunar-forming impacts: High-resolution SPH and AMR-CTH simulations, *Icarus, 222*, pp. 200-219.

[19] Crawford, D.A*.,* 2011, *42nd Lunar and Planetary Sci. Conf.*, Abs. #2112 (http://www.lpi.usra.edu/meetings/lpsc2011/pdf/2112.pdf).

[20] Crawford, D. A. and Schultz, P. H., 1988, Laboratory observations of impact-generated magnetic fields, *Nature, 336*, pp. 50-52.

[21] Crawford, D. A. and Schultz, P. H., 1991, Laboratory Investigations of Impact-Generated Plasma, *Journal of Geophysical Research, 96*, pp. 18,807-18,817.

[22] Crawford, D. A. and Schultz, P. H., 1993, The Production and Evolution of Impact-Generated Magnetic Fields, *International Journal of Impact Engineering*, *14*, pp. 205-216.

[23] Crawford, D. A. and Schultz, P. H., 1999, Electromagnetic Properties of Impact-Generated Plasma, Vapor and Debris, *International Journal of Impact Engineering, Vol.* 23, pp. *169-180.*

[24] Crawford, D. A., 2015, Computational modeling of electrostatic charge and fields produced by hypervelocity impact, *Proceedings of the 13th Hypervelocity Impact Symposium*, *Procedia Engineering*, *Vol. 103*, pp 89-96.

[25] Crawford, D. A., 2019, Simulations of Magnetic Fields Produced by Asteroid Impact: Possible Implications for Planetary Paleomagnetism, *Proceedings of the 15th Hypervelocity Impact Symposium*, this volume.